Analytical and numerical study on a vortex sheet in incompressible Richtmyer-Meshkov instability in cylindrical geometry

Chihiro Matsuoka[1]

[1]*Department of Physics, Ehime University, 2-5, Bunkyocho, Matsuyama, Ehime 790-8577, Japan*

Katsunobu Nishihara[2]

[2]*Institute of Laser Engineering, Osaka University, 2-6, Yamada-oka Suita, Osaka, 565-0871, Japan*

Motion of a fluid interface in the Richtmyer-Meshkov instability in cylindrical geometry is examined analytically and numerically. Nonlinear stability analysis is performed in order to clarify the dependence of growth rates of a bubble and spike on the Atwood number and mode number n involved in the initial perturbations. We discuss differences of weakly and fully nonlinear evolution in cylindrical geometry from that in planar geometry. It is shown that the analytical growth rates coincide well with the numerical ones up to the neighborhood of the break down of numerical computations. Long-time behavior of the fluid interface as a vortex sheet is numerically investigated by using the vortex method and the roll up of the vortex sheet is discussed for different Atwood numbers. The temporal evolution of the curvature of a bubble and spike for several mode numbers is investigated and presented that the curvature of spikes is always larger than that of bubbles. The circulation and the strength of the vortex sheet at the fully nonlinear stage are discussed, and it is shown that their behavior is different for the cases that the inner fluid is heavier than the outer one and vice versa.

I. INTRODUCTION

When converging or diverging cylindrical shock waves interact with a circular fluid interface with different densities, small initial spatial perturbations grow under the Richtmyer-Meshkov instability (RMI) [1]. The corrugated interface deforms such as petals, and finally, each petal rolls up to a mushroomlike structure [2–4]. Understanding of this phenomenon is important in various areas such as astrophysical supernova, supersonic combustion and the ignition of a central hot spot in inertial confinement fusion [5]. Zhang and Graham [2] investigated RMI in cylindrical geometry with the use of hydrodynamic simulations and calculated the nonlinear growth of an interface driven by shock waves with various Mach numbers showing a scaling law for a fixed Atwood number and mode number. Zhakhovskii *et al.* [3] observed the roll up of the circular interface using molecular dynamic (MD) simulations with converging cylindrical shock waves. Experimentally, RMI is generated in shock tubes, in which a flat [6] or cylindrical [7–9] interface separated by two gases is accelerated by a plane or cylindrical shock wave. However, the existence of shock waves is not essential to generate RMI but the instability can be caused if only the nonuniform vorticity exists on the interface [10,11]. This nonuniform vorticity concentrates to vortex cores, i.e., the center of the roll up, and that leads to the mushroomlike structure at the fully nonlinear stage [12].

In addition to the convergence effects there are many features in cylindrical geometry, such as existence of two independent spatial scales, i.e., the radius and wavelength, and also the ingoing and outgoing motion of bubbles and spikes. We will show that these geometrical complexities essentially determine fully nonlinear growth of the instability. In the nonlinear phase, the vortex interaction is nonlocal. There-fore, the interaction in cylindrical geometry may not be the same as that in an infinite periodic planar case. As will be shown, the nonlinear evolution of the vortex sheet is quite different for modes 1, 2 and higher. Here, we restrict ourselves to inviscid and incompressible fluids, and neither implosion nor explosion of the circular interface. Also initial vorticity is nonuniformly distributed only at the interface. Despite these restrictions the study reveals many features of the nonlinear growth in cylindrical geometry.

In the previous paper [4], we have numerically investigated motion of the fluid interface in RMI with cylindrical geometry by regarding the interface as a cylindrical vortex sheet. In that work we have shown nonlinear evolution of the interfacial profiles with various mode numbers, growth rates of bubbles and spikes and the peak-to-valley amplitudes of the interface for two Atwood numbers with the same absolute value, where the sign of the Atwood number differs depending on whether the inner fluid, with respect to the interface, is heavier than the outer one or vice versa. Unlike the planar RMI, the nonlinear growth rate strongly depends on mode numbers in cylindrical geometry and the dynamics of the interface is determined from the inward and outward motion with respect to the interface rather than from bubble and spike, especially for low modes.

In this article we investigate motion of the fluid interface in RMI with cylindrical geometry both analytically and numerically. In the analytical treatment, we adopt the Bernoulli equation (2.1) and the kinematic boundary conditions (2.2) and (2.3) as the governing equations, and perform the weakly nonlinear analysis [11,13] up to the third order. In the numerical study, we use the vortex method [4,12,14,15] and investigate the long-time behavior of the vortex sheet by solving the equation for the vortex induced velocity derived from the Biot-Savart integral, together with an equation of

the temporal evolution of the strength of the vortex sheet derived from the Bernoulli equation (3.1). The evolution equation for the sheet strength and the equation for the vortex induced velocity adopted in numerical calculations correspond to the Bernoulli equation and the kinematic boundary conditions in the analytical treatment, respectively. With this vortex sheet approach, the temporal evolution of curvatures of bubbles and spikes, the circulation (net vorticity) and the sheet strength are calculated in addition to interfacial profiles for larger Atwood numbers than the one adopted in the previous paper [4].

This article consists of four sections. In Sec. II, we perform the weakly nonlinear analysis and present the comparison of the growth rates of bubbles and spikes between the analytical solutions and the numerical ones for various modes and Atwood numbers. In Sec. III, we investigate the long-time behavior of a vortex sheet by numerical calculations using the vortex method. We present the temporal evolution of curvature of bubble and spike, the asymptotic behavior of the circulation and sheet strength of the vortex sheet. In addition to that, we show the difference of growth rates of bubbles and spikes due to the difference of Atwood numbers. Section IV is devoted to conclusion.

II. ANALYTICAL RESULTS

A. Weakly nonlinear analysis for governing equations

In this section we investigate the nonlinear stability of governing equations. We will show the dependence of growth rates of a bubble and spike on mode number n or Atwood number A, where we define the Atwood number A as $A=(\rho_2-\rho_1)/(\rho_1+\rho_2)$ for two fluid densities ρ_i $(i=1,2)$. Throughout this paper, we determine the subscripts $i=1$ and $i=2$ correspond to the inner and outer fluids, therefore, $A>0$ and $A<0$ correspond to a case of light inner fluid and heavy outer fluid, and vice versa.

Governing equations needed in the weakly nonlinear analysis are the Bernoulli equation and kinematic boundary conditions. The Bernoulli equation at the interface in the circular coordinate system (r,θ) is given by

$$\rho_1\left\{\frac{\partial\phi_1}{\partial t}+\frac{1}{2}\left[\left(\frac{\partial\phi_1}{\partial r}\right)^2+\frac{1}{r^2}\left(\frac{\partial\phi_1}{\partial\theta}\right)^2\right]\right\}$$
$$=\rho_2\left\{\frac{\partial\phi_2}{\partial t}+\frac{1}{2}\left[\left(\frac{\partial\phi_2}{\partial r}\right)^2+\frac{1}{r^2}\left(\frac{\partial\phi_2}{\partial\theta}\right)^2\right]\right\}, \quad (2.1)$$

where the velocity potential ϕ_i is related with the fluid velocity $\boldsymbol{u}_i$ as $\boldsymbol{u}_i=\boldsymbol{\nabla}\phi_i$ in each region i. The circular boundary $F=r-\eta(\theta,t)=0$ satisfies the kinematic boundary condition $dF/dt=0$, i.e.,

$$\frac{\partial\eta}{\partial t}=\frac{\partial\phi_1}{\partial r}-\frac{1}{r^2}\frac{\partial\eta}{\partial\theta}\frac{\partial\phi_1}{\partial\theta}, \quad (2.2)$$

$$\frac{\partial\eta}{\partial t}=\frac{\partial\phi_2}{\partial r}-\frac{1}{r^2}\frac{\partial\eta}{\partial\theta}\frac{\partial\phi_2}{\partial\theta}, \quad (2.3)$$

where all quantities in Eqs. (2.1)–(2.3) are estimated at the boundary $r=r_0$, where r_0 is the initial radius of the interface.

Since the system is assumed to be incompressible, the velocity potential ϕ_i satisfies the Laplace equation

$$\triangle\phi_i=0,$$

in each fluid region $i(i=1,2)$. We can obtain the continuity condition of normal velocities of two fluids and the displacement $\eta(\theta,t)$ with respect to the normal direction by subtracting Eq. (2.2) from Eq. (2.3) and adding Eq. (2.2) multiplied by ρ_1 to Eq. (2.3) multiplied by ρ_2, respectively.

We replace η, ϕ_i, r and time t in Eqs. (2.1)–(2.3) to dimensionless variables $\eta\rightarrow\eta/r_0$, $\phi_i\rightarrow\phi_i/(r_0v_0)$, $r\rightarrow r/r_0$, and $t\rightarrow tv_0/r_0$, where v_0 is the initial growth rate which corresponds to the linear growth rate of RMI for the wavelength $\lambda=2\pi r_0/n$ with mode number n [4]. With these dimensionless variables, we expand ϕ_i and η in Eqs. (2.1)–(2.3) with a formal expansion parameter ϵ $(\epsilon\ll1)$:

$$\phi_i=\epsilon\phi_i^{(1)}+\epsilon^2\phi_i^{(2)}+\cdots,$$

$$\eta=1+\epsilon\eta^{(1)}+\epsilon^2\eta^{(2)}+\cdots, \quad (2.4)$$

where ϕ_i are expanded taking into account that ϕ_i are solutions of the Laplace equation given by

$$\phi_1=\sum_{m=1}^{\infty}\epsilon^m\phi_1^{(m)}\ (r<r_0)=\sum_{m=1}^{\infty}\epsilon^m\sum_{l=0}^{\left[\frac{m+1}{2}\right]}B_{1,m-2l}^{(m)}(t)$$
$$\times\left(\frac{r}{r_0}\right)^{(m-2l)n}\cos(m-2l)n\theta,$$

$$\phi_2=\sum_{m=1}^{\infty}\epsilon^m\phi_2^{(m)}\ (r>r_0)=\sum_{m=1}^{\infty}\epsilon^m\sum_{l=0}^{\left[\frac{m+1}{2}\right]}B_{2,m-2l}^{(m)}(t)$$
$$\times\left(\frac{r}{r_0}\right)^{-(m-2l)n}\cos(m-2l)n\theta, \quad (2.5)$$

where Gauss's symbol $[(m+1)/2]$ denotes the maximum integer which does not exceed $(m+1)/2$ and $B_{i,m-2l}^{(m)}(t)$ is the amplitude of the Fourier mode of $(m-2l)$-th order in the mth order of ϵ. Note that higher modes arises due to nonlinear mode coupling. Expanding ϕ_i at normalized initial radius $r=1$ as

$$\phi_i=\phi_i+\left.\frac{\partial\phi_i}{\partial r}\right|_{r=1}\eta+\frac{1}{2}\left.\frac{\partial^2\phi_i}{\partial r^2}\right|_{r=1}\eta^2+\cdots,$$

and substituting Eqs. (2.4) and (2.5) into Eqs. (2.1)–(2.3), we obtain at the first order $O(\epsilon)$

$$\eta^{(1)}=(t+a_0)\cos n\theta, \quad (2.6)$$

at the second order $O(\epsilon^2)$

$$\eta_2^{(2)}=-\frac{t^2}{2}\left(An+\frac{1}{2}\right)\cos 2n\theta,$$

$$\eta_0^{(2)}=-\frac{t^2}{4},$$

$$\eta^{(2)} = \eta_2^{(2)} + \eta_0^{(2)}, \tag{2.7}$$

and at the third order $O(\epsilon^3)$

$$\eta_1^{(3)} = -\left[\frac{t^3}{24}[(4A^2+1)n^2 - 4An - 9]\right.$$
$$\left. + \frac{a_0 t^2}{8}(n^2+An-6)\right]\cos n\theta,$$

$$\eta_3^{(3)} = \left[\frac{t^3}{8}((4A^2-1)n^2+4An+1)\right.$$
$$\left. - \frac{a_0 t^2}{8}(3n^2-5An-2)\right]\cos 3n\theta,$$

$$\eta^{(3)} = \eta_1^{(3)} + \eta_3^{(3)}, \tag{2.8}$$

where a_0 is the normalized initial amplitude a_0/r_0 and we imposed here the initial condition $\eta(\theta,0)=a_0\cos n\theta$ and $\partial\eta(\theta,0)/\partial t=\cos n\theta$, as given in Eq. (2.6). It should be noted that other higher order terms are set to be zero. Setting the formal expansion parameter $\epsilon=1$, we obtain the analytic solution $r=\eta$ due to the weakly nonlinear analysis up to the third order

$$\eta = 1 + \eta^{(1)} + \eta^{(2)} + \eta^{(3)}. \tag{2.9}$$

We would here mention the difference of the perturbation amplitudes η between cylindrical geometry and planar geometry. The nonoscillation part $\eta_0^{(2)}$ in Eq. (2.7) does not appear in the planar geometry [13], however, it is important in the cylindrical geometry. The existence of the nonoscillation term guarantees the conservation of the area surrounded by the interface because of the assumption of incompressible fluids (see Appendix A). The area preservative property also produces the asymmetrical shape of the outgoing and ingoing perturbations even for $A=0$ in cylindrical geometry, since the second order term $\eta^{(2)}$ remains to be finite for $A=0$. Here, the words "outgoing" and "ingoing" indicate the parts of the interface which move toward the outer and the inner looking from the initial boundary, respectively [4]. The asymmetrical property of the interface profile even for $A=0$ in cylindrical geometry can be also found at the fully nonlinear stage in the numerical calculation [see Fig. 4(a)]. The second order term $\eta^{(2)}$ and subsequent higher order nonoscillation terms in the perturbation expansions can be derived from the area preservative property alone, without Eqs. (2.1)–(2.3). Systematic derivation for these terms is presented in Appendix A. Not only the second order term $\eta^{(2)}$ but also all even orders $\eta^{(4)}, \eta^{(6)}, \ldots, \eta^{(2m)}, \ldots, (m=1,2,\ldots)$ do not vanish even when $A=0$ in cylindrical geometry, although they vanish in planar geometry [13].

However, the perturbation amplitudes in the weakly nonlinear theory in cylindrical geometry should converge to that in planar geometry for a very short wavelength compared with the radius, namely, for $\lambda=2\pi r_0/n \ll r_0$, and for small time t. The term proportional to n in the second order amplitude given by Eq. (2.7) and the terms proportional to n^2 in the third order amplitude given by Eq. (2.8) dominate in each

order for the large mode numbers n. It should be noted that those dominant terms, i.e., $-(Ant^2)/2$ in $\eta_2^{(2)}$, $-[(4A^2+1)n^2t^3]/24$ and $-(a_0n^2t^2)/8$ in $\eta_1^{(3)}$, and $[(4A^2-1)n^2t^3]/8$ and $-(3a_0n^2t^2)/8$ in $\eta_3^{(3)}$ coincide with the corresponding terms in planar geometry in Ref. [13]. This fact indicates that the nonlinear evolution of the interface in cylindrical geometry is analogous to that in planar geometry for large modes n and short time t. However, for small mode numbers n, the other terms cannot be ignored and the perturbation growth in cylindrical geometry differs from that in planar geometry.

For $A>0$ ($A<0$), the outgoing parts of the perturbation, $\theta=(2m\pi)/n$ and its ingoing parts $\theta=(1+2m)\pi/n$ ($m=0,\ldots,n-1$) correspond to bubbles (spikes) and spikes (bubbles), respectively. The growth rates of the outgoing perturbation and ingoing perturbation are, respectively, calculated from time derivative of the perturbation amplitudes as

$$\left.\frac{\partial\eta(t)}{\partial t}\right|_{\text{out}} = 1 - t(An+1) - \left[\frac{t^2}{2}[(1-2A^2)n^2+4An+3]\right.$$
$$\left. + a_0t(n^2-An-2)\right] \tag{2.10}$$

and

$$\left.\frac{\partial\eta(t)}{\partial t}\right|_{\text{in}} = -1 - t(An+1) + \left[\frac{t^2}{2}[(1-2A^2)n^2+4An+3]\right.$$
$$\left. + a_0t(n^2-An-2)\right], \tag{2.11}$$

for mode n.

In Eqs. (2.10) and (2.11) the positive and negative values of the growth rates correspond to the outgoing growth and ingoing growth, respectively. In cylindrical geometry the nonlinear growth rates depend on the sign of A even for the same linear growth rate. It should also be noted that the second terms in Eqs. (2.10) and (2.11) results in the difference of the growth rate between the outgoing and ingoing perturbations within the weakly nonlinear theory. For Atwood number and mode that satisfy the condition of $(An+1)>0$ the ingoing growth rate is always larger than the outgoing growth rate at least for small time t. However, as will be shown later, in the fully nonlinear stage the ingoing growth rates asymptotically tend to zero, while the outgoing growth rates remain finite.

For the comparison with numerical results, we define the circulation Γ as $\Gamma=\phi_1-\phi_2$. We have at $O(\epsilon)$

$$\Gamma^{(1)} = -2\cos n\theta, \tag{2.12}$$

at $O(\epsilon^2)$

$$\Gamma^{(2)} = At\cos 2n\theta, \tag{2.13}$$

and at $O(\epsilon^3)$

$$\Gamma^{(3)} = \frac{1}{2}\{[(2A^2-1)n+A]t^2 + (3A-2n)a_0t\}\cos n\theta$$
$$- \frac{1}{2}\{[(2A^2+1)n+A]t^2 + (A+2n)a_0t\}\cos 3n\theta,$$
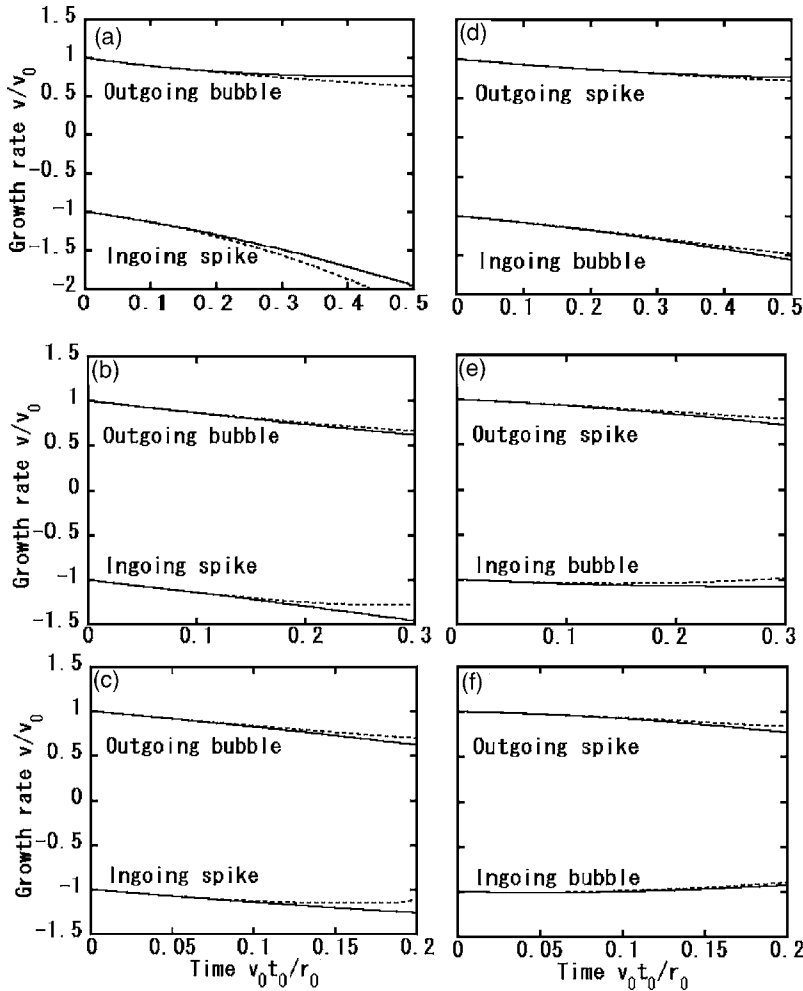
FIG. 1. Comparison of analytical and numerical growth rates of bubbles and spikes for (a) $n=1$, (b) $n=2$, (c) $n=3$ for $A=0.2$ and (d)–(f) for the same modes for $A=-0.2$. Solid and dashed lines denote analytical and numerical ($\delta=0$) results, respectively.

$$\Gamma = \Gamma^{(1)} + \Gamma^{(2)} + \Gamma^{(3)}. \qquad (2.14)$$

Since the second order circulation is proportional to Atwood number A, the circulation increases at the tip of the spike, while it decreases at the tip of the bubbles independently the sign of A. This is the same as planar case. However the terms not proportional to mode number n in the third order do not appear in planar geometry. Since they are proportional to A, difference in the circulation appears in later time depending on the sign of Atwood number A.

B. Comparison of analytical and numerical results

We show the comparison of analytical and numerical growth rates of bubbles and spikes for Atwood number A $=\pm 0.2$ and modes $n=1$, 2 and 3 in Fig. 1. We set $a_0=0$ throughout this paper, i.e., the initial interface is a circle with radius $r=1$. We choose the regularized parameter δ introduced by Krasny [16] as $\delta=0$ for the numerical calculations (see Sec. III and Appendix B for details). Time in the figures is taken up to the neighborhood of the break-down of numerical calculations for each mode. When we normalize time t by the wavelength λ, time in the planar RMI t_p is given by $t_p=2\pi v_0 t/\lambda=n v_0 t/r_0$ and the break-down time is almost the same at planar time; $t_p=0.5-0.6$ for all modes in Figs. 1–3.

As we see from Fig. 1, analytical and numerical growth rates coincide well with each other for all modes. When the normalized time t approaches the break-down time t_b for each mode, the difference between analytical and numerical results becomes obvious due to the growth of higher Fourier modes in numerical calculations. The difference between analytical and numerical results is smaller for $A=-0.2$ than for $A=0.2$. For modes $n=1$, the break-down time is t_b $=0.52$ for $A=-0.2$ and $t_b=0.63$ for $A=-0.2$. The difference between analytical and numerical solutions for mode $n=1$ and $A<0$ is smaller than that for $A>0$ even at their breakdown times. Figure 1 shows that the growth rates of a spike is not necessarily larger than that of a bubble as found in the planar RMI [12,15] at least for $(An+1)>0$. For cylindrical geometry, the growth rates are determined from the ingoing and outgoing motion rather than from bubble or spike.

Figure 2 shows analytical and numerical growth rates for mode $n=8$ and Atwood numbers $A=\pm 0.2$ and $A=\pm 0.6$. This figure also guarantees that our numerical calculations are accurate for larger Atwood numbers, and at the same time, we see that the weakly nonlinear analysis up to the third order approximates the solutions well for every mode and the Atwood numbers. We can hardly distinguish the numerical results from the analytical ones for $A=\pm 0.2$ up to the breakdown time of the computations (the break-down time t_b is approximately 0.07 for this mode). The growth rate of out-
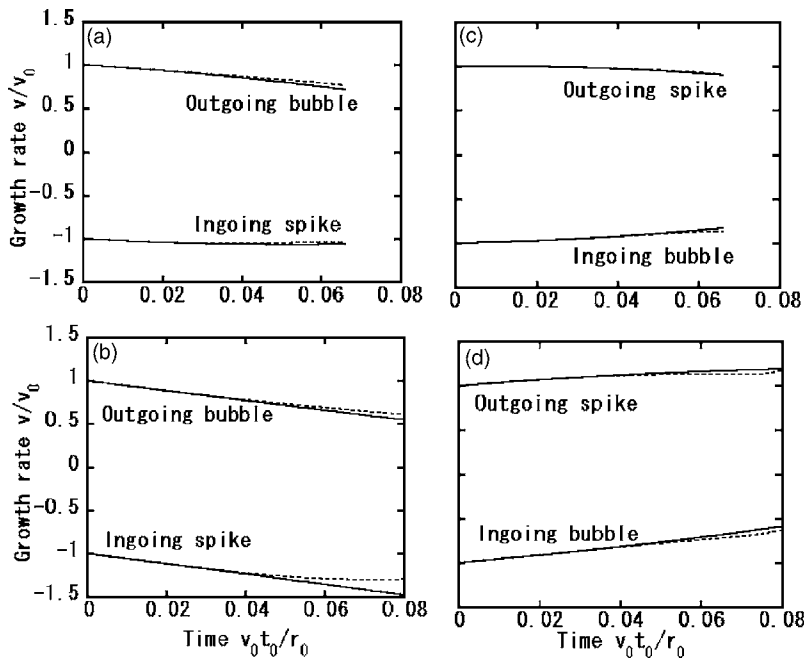
FIG. 2. Comparison of analytical and numerical growth rates of bubbles and spikes for mode $n=8$ and Atwood numbers (a) $A=0.2$, (b) $A=0.6$, (c) $A=-0.2$, and (d) $A=-0.6$, where solid and dashed lines denote analytical and numerical ($\delta=0$) results, respectively.

going bubble for $A=0.6$ is almost the same with smaller Atwood numbers, while the absolute value of the growth rate of ingoing spike is larger for larger Atwood numbers at a fixed time. For $A=-0.6$, the Atwood number dependence appears clearer on outgoing spikes, i.e., the growth rates of outgoing spikes is larger for larger Atwood numbers. This tendency appears in all mode numbers when $A<0$. For larger Atwood numbers in their absolute values, the nonlin-
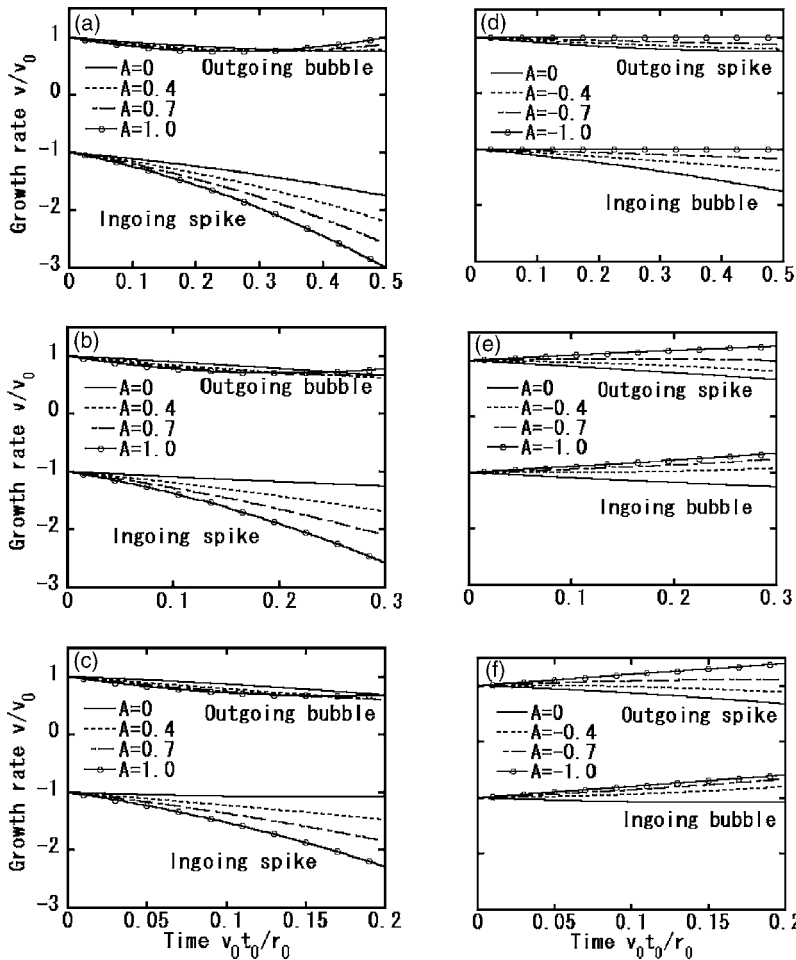
FIG. 3. Analytical growth rates of bubbles and spikes for various Atwood numbers and modes; (a) $n=1$, (b) $n=2$, (c) $n=3$ for $A=0$, 0.4, 0.7, 1.0 and (d)–(f) for the same modes for $A=0$, -0.4, -0.7, -1.0, where solid, dashed, dot-dashed lines, and solid lines with circles denote $A=0$, ±0.4, ±0.7, and ±1.0, respectively

ear growth rates of a spike is larger than 1 in its absolute value, while that of a bubble is smaller than 1 regardless of ingoing or outgoing [see Figs. 2(b) and 2(d)]. This tendency, especially for ingoing spikes is also found in lower modes (see Fig. 3).

We show analytical growth rates for various Atwood numbers for modes $n=1$, 2, and 3 in Fig. 3. It is not easy to perform numerical calculations for larger Atwood numbers $A \gtrsim 0.7$ in cylindrical geometry, however, the analytical solution gives the growth rates ranging from $A=0$ to $A=\pm 1$. The Atwood number dependence are more apparent on spikes for both $A>0$ and $A<0$, especially for ingoing spikes for $A>0$, while outgoing bubbles for $A>0$ are hardly affected by the Atwood number. When $A>0$, the first and second order $\partial \eta^{(1)}/\partial t$ and $\partial \eta^{(2)}/\partial t$ of the ingoing spikes are both negative and the sign of the leading term $\partial \eta_3^{(3)}/\partial t$ at the third order $\partial \eta^{(3)}/\partial t$ is also negative for larger Atwood numbers. Therefore, ingoing spikes diverge in the negative direction as shown in the figure. When $A=-1.0$ and $n=1$ [Fig. 3(d)], the growth rates of a bubble and spike remains approximately 1 in its absolute value. This is also confirmed by the fact that the nonlinear terms $\eta^{(2)}=0$ in Eq. (2.7).

III. NUMERICAL RESULTS

In this section we regard the circular interface in RMI as a cylindrical vortex sheet and investigate its long-time behavior with the vortex method. The equations that we solve here are a coupled system with respect to (r, θ, κ) [4]:

$$r_t = q^r + \frac{\alpha \kappa r_\beta}{2 s_\beta},$$

$$r \theta_t = q^\theta + \frac{\alpha \kappa r \theta_\beta}{2 s_\beta},$$

$$\kappa_t = -\frac{2A}{s_\beta}(r_\beta q_t^r + r \theta_\beta q_t^\theta) - \frac{(1-\alpha A)}{s_\beta^2} \kappa [(r_\beta q_\beta^r + r \theta_\beta q_\beta^\theta) + (rq^r \theta_\beta^2 - r_\beta \theta_\beta q^\theta)] - \frac{A-\alpha}{4 s_\beta}(\kappa^2)_\beta, \quad (3.1)$$

where

$$q^r = \frac{-1}{2\pi} \int_0^{2\pi} \frac{\kappa'[r'\sin(\theta-\theta')]s_\beta' d\beta'}{r^2 - 2rr'\cos(\theta-\theta') + r'^2},$$

$$q^\theta = \frac{1}{2\pi} \int_0^{2\pi} \frac{\kappa'[r - r'\cos(\theta-\theta')]s_\beta' d\beta'}{r^2 - 2rr'\cos(\theta-\theta') + r'^2},$$

is the vortex induced velocity in this system (for the derivation of those equations, see Appendix B). Here, α is an artificial parameter for numerical computations [4,11], β is a Lagrangian parameter which parametrizes the interface as $[r(\beta), \theta(\beta)]$, $s_\beta = \sqrt{r_\beta^2 + r^2 \theta_\beta^2}$, where the subscript denotes the differentiation with respect to the variable and the variables with the prime denote that they are functions with respect to β'. The sheet strength κ is related to the circulation $\Gamma = \phi_1$

$-\phi_2$ as $\kappa = d\Gamma/ds$. Numerical methods for solving Eq. (3.1) are also presented in Appendix B.

In numerical calculations, we also use the same normalization for the variables which we introduced in Sec. II. Throughout this section, the normalized initial conditions are given as

$$r(\beta, 0) = 1, \quad \theta(\beta, 0) = \beta,$$

$$\kappa(\beta, 0) = 2\sin(n\beta),$$

for all mode number n. The regularized parameter δ is chosen that $\delta = 0.1$ for all calculations $\delta \neq 0$. When we take smaller δ, the roll-up of a vortex sheet occurs at earlier time and when we take larger δ, that occurs at later time. This tendency is also observed for planar geometry [12]. Throughout this paper, the number of grid points N is taken that $N = 256n$ for mode number n.

A. Atwood number dependence on growth rates

Figure 4 shows interfacial profiles for mode $n=3$ and Atwood number $A=0$, ± 0.2, and ± 0.4. We choose the factor $\alpha = \mp A^2$ for $A = \pm 0.2$ and $\alpha = \mp 0.04$ for $A = \pm 0.4$, and the time step $\triangle t = 0.00025$ for all calculations including $A=0$. If we take larger α, e.g., $\alpha = -A^2$ $(\alpha = A^2)$ for $A>0$ $(A<0)$, the calculation for $A=0.4$ breaks down at earlier time, although the result for $A=-0.4$ is unchanged. As shown in Fig. 4, the profile of the outgoing bubbles (ingoing spikes) for $A>0$ is not so different from those of the outgoing spikes (ingoing bubbles) for $A<0$. The interface profile in cylindrical geometry is, therefore, determined mainly from either outgoing or ingoing growth, regardless of the bubbles and spikes at least for small mode number. The shape of the outgoing parts and ingoing parts of the interface is not symmetric with each other even for $A=0$. The winding of the roll up is tightest for $A=0$ and that becomes looser as the Atwood number becomes larger for both $A>0$ and $A<0$. The penetration depth of the spike into light fluid increases with the increase of $|A|$, while that of the bubble into heavy fluid decreases.

Asymptotic growth rates of bubbles and spikes for $A=0$, ± 0.2, and ± 0.4 are depicted for mode $n=3$ in Fig. 5. For very small normalization time t, the growth rates of bubbles and spikes deviate from the analytical value of ± 1, due to the finiteness of δ, therefore, we have shown those within $0.2 \leq t \leq 1.8$ here. We see that the ingoing growth rates for both bubbles and spikes decrease rapidly and tend to zero independent of the Atwood number, while the decrease in outgoing growth rates are relatively slow and they keep some constant values even when the ingoing growth rates are close to zero. As the Atwood number $|A|$ becomes larger, the growth rates of a spike becomes larger, while the growth rates of a bubble becomes smaller regardless of ingoing or outgoing. This trend is also true at earlier stages [see Figs. 3(c) and 3(f)]. For the dependence of growth rates on modes for a fixed Atwood number ($|A|=0.2$), refer to Ref. [4]. We mention that the tendency found in Fig. 2 in this reference is unchanged even for larger Atwood numbers.
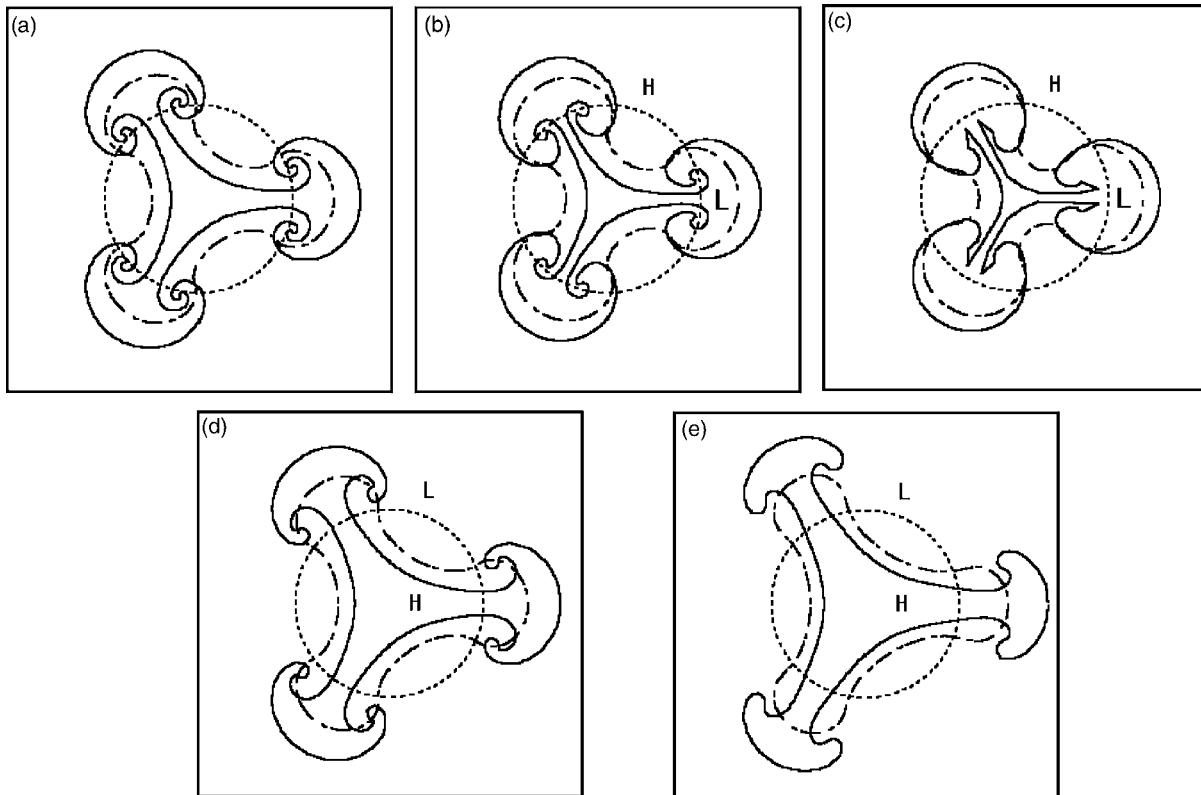
FIG. 4. Interfacial profiles for mode $n=3$; (a) $A=0$, (b) $A=0.2$, (c) $A=0.4$, (d) $A=-0.2$, and (e) $A=-0.4$, where dashed, dot-dashed, and solid lines depict $t=0$, $t=0.8$, and $t=1.8$, respectively. All box sizes in the figures are $|x| \leq 2.0$ and $|y| \leq 2.0$. The letters "H" and "L" denote heavy and light fluids, respectively.

B. Curvature, circulation, and sheet strength

Although the bubble curvature has been predicted to be asymptotically zero in planar geometry [17], it cannot be zero in cylindrical geometry. In Fig. 6 we show temporal evolution of curvatures of bubble and spike. The curvature is given by the following form:

$$[\theta_\beta(2r_\beta^2 + r^2\theta_\beta^2) + r(r_\beta\theta_{\beta\beta} - \theta_\beta r_{\beta\beta})]/s_\beta^{3/2},$$

where the derivatives are calculated by using their Fourier series expansions [12]. The regularized parameter δ is taken that $\delta=0$ for $n=1$ and $\delta=0.1$ for other modes. For the corresponding interfacial profiles, refer to Ref. [4]. For $n=1$, the curvature of the ingoing part (spike) for $A=0.2$ becomes negative, however, the ingoing part for $A=-0.2$ keeps a positive sign at least until the break-down of the computation (see profiles in Fig. 1 in Ref. [4]). For all modes $n \geq 3$, the curvature of ingoing bubble and spike becomes negative, namely, concave profile looking from the inside of the interface within relatively early time, even if their initial value is one. It is interesting that the absolute values of the curvature then increase once and slowly decrease independently of ingoing or outgoing and bubble or spike. The curvature of both the outgoing and ingoing spikes is slightly larger than that of the ingoing and outgoing bubbles in its absolute value even in cylindrical geometry, although it is not clear from Fig. 6. Their asymptotic values do not depend much on the Atwood number, but only on the mode number. If we divide the curvatures by the mode number, their absolute values are almost
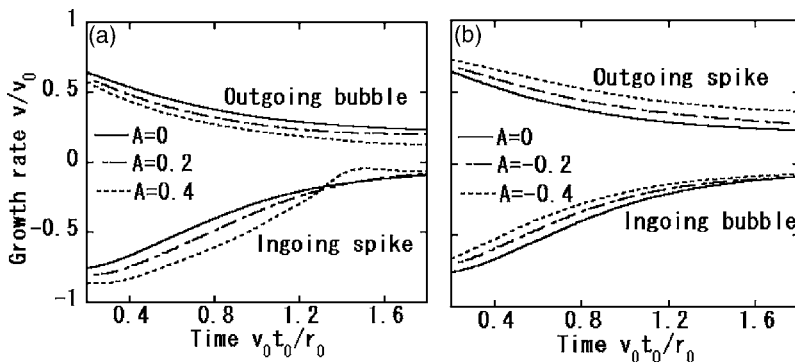
FIG. 5. Asymptotic growth rates of bubbles and spikes for mode $n=3$; (a) $A=0$, 0.2, 0.4 and (b) $A=0$, -0.2, -0.4, where solid, dot-dashed, and dashed lines depict $A=0$, ± 0.2, and ± 0.4, respectively. Time is taken over $0.2 \leq t \leq 1.8$.
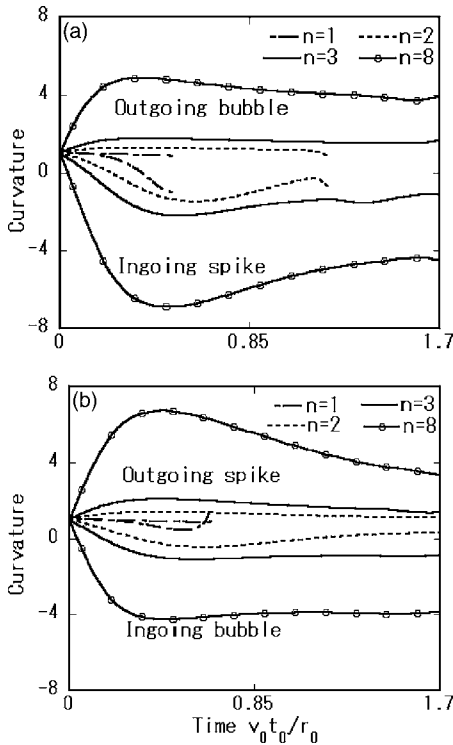
FIG. 6. Temporal evolution of curvatures of bubbles and spikes for various modes for (a) $A=0.2$ and (b) $A=-0.2$. Dot-dashed, dashed, solid, and solid with circles lines denote $n=1$, $n=2$, $n=3$, and $n=8$, respectively.

the same, approximately the normalized value of 0.5, for $n \geq 3$.

Figure 7 shows the circulation Γ and the sheet strength κ for modes $n=1$ and 3, and $A=\pm 0.2$. The calculations are performed with $\delta=0$, $\alpha=-A$ ($\alpha=A$) for $A>0$ ($A<0$) when $n=1$, and $\delta=0.1$, $\alpha=-A^2$ ($\alpha=A^2$) for $A>0$ ($A<0$) when $n=3$, respectively. Unlike the Kelvin-Helmholtz instability, the Kelvin's circulation theorem $d\Gamma/dt=0$ does not hold in

RMI except the special case $A=0$. For $A=0$, the circulation Γ kept its initial value $\Gamma(\beta,0)=-2\cos(n\beta)$ up to the break-down time in our calculations for all modes. The circulation Γ has its maximum (minimum) value at the tip of the spike and its minimum (maximum) value at the tip of the bubble for $A>0$ and ($A<0$). The circulation changes more smoothly with the Lagrangian parameter β near the tip of the bubbles than that near the tip of the spikes. It should be also mentioned that the variation of the circulation with respect to the Lagangian parameter β is not the same for the outgoing bubble ($A>0$) and the ingoing bubble ($A<0$), as seen for mode $n=3$ in Fig. 7.

A pair of sharp peaks with opposite signs observed in κ correspond to vortex cores, the centers of roll-up [12]. Two peaks in a pair near spikes for $A=0.2$ and mode $n=3$ seem to be very close in the Lagrangian coordinate β. However, they are considerably separated with each other in the interfacial profile as shown in Fig. 4(b). This situation is also the same in another modes for $A=0.2$. For $A=-0.2$, two peaks in a pair near spikes are relatively close each other in both La-grangian coordinate and interfacial profile [see Fig. 4(d)]. When we fix the mode number n, the absolute value of the peak in κ at a fixed time is larger for $A>0$ than that for $A<0$ for the same Atwood number in its absolute value. As the mode number n (≥ 2) increases, this peak value tends to be smaller in its absolute value for both $A>0$ and $A<0$. When the mode number and time were both fixed, little dif-ferences in the peak values between $A=0.2$ ($A=-0.2$) and $A=0.4$ ($A=-0.4$) were found in our computations, although we could not calculate whether that is also true or not for larger Atwood numbers. We have also observed that the peak value of κ for $A=0$ and mode $n=3$ is approximately ± 5.2, which is larger than those for $A=\pm 0.2$. However, the second vorticity by the baroclinic effect [12], i.e., smaller peaks in the neighborhood of the sharp peak in κ found in (b) and (d) in Fig. 7 [see also (a) in Fig. 8] does not appear for $A=0$.

In Fig. 8, we show the circulation and sheet strength in the planar RMI together with the interfacial profile at the
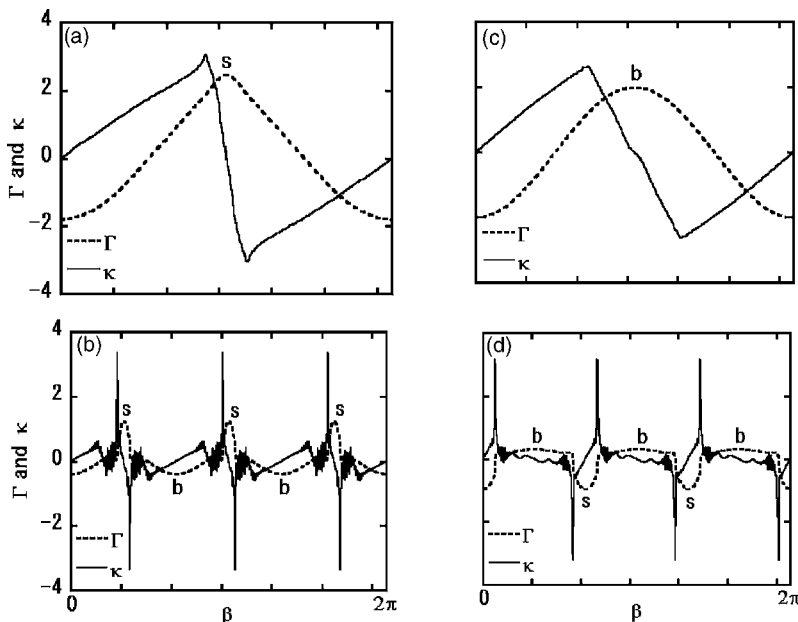
FIG. 7. Circulation Γ and sheet strength κ at the fully nonlinear stage; (a) $n=1$, $t=0.52$, (b) $n=3$, $t=2.0$ for $A=0.2$ and (c) $n=1$, $t=0.63$, (d) $n=3$, $t=2.0$ for $A=-0.2$. Dashed and solid lines denote the circulation Γ and the strength κ, re-spectively. The letters "b" and "s" denote the po-sition of bubble and spike, respectively, where both $\beta=0$ and 2π correspond to bubble for $A=0.2$ and spike for $A=-0.2$ (not marked in the figure).
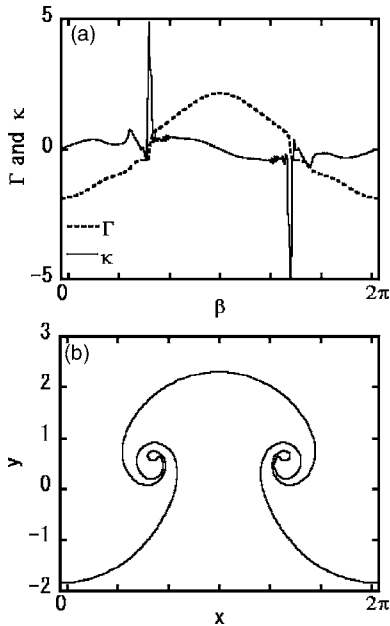
FIG. 8. Circulation and sheet strength in the planar RMI for $A=0.2$ and $t_p=4.2$; (a) circulation Γ and sheet strength κ, where dashed and solid lines denote Γ and κ, respectively, and (b) interfacial profiles at the corresponding time.

corresponding time for the comparison of cylindrical RMI. Here, the Atwood number $A=0.2$ and time $t_p=4.2$, which approximately corresponds to time $t=2.0$ for mode $n=3$ in the cylindrical geometry. The initial configurations of the plane vortex sheet are given by

$$x(\beta,0) = \beta, \quad y(\beta,0) = 0,$$

$$\kappa(\beta,0) = -2\sin\beta,$$

where the upper fluid of the interface (fluid 1) is lighter than the lower fluid (fluid 2) in the figure. When we take $A \to -A$ and $\alpha \to -\alpha$, or $\kappa \to -\kappa$ remaining the signs of A and α in the governing equations unchanged, the positions of the bubble and spike reverse, however, the shape and value at bubble and spike in Γ and κ is unchanged. The peak value in κ in planar geometry is larger than those for $A=\pm0.2$ in cylindrical geometry and the winding of the roll-up (b) is tighter than the counterparts for $A=\pm0.2$ in cylindrical geometry at the corresponding time [4] (see also Fig. 4).

IV. CONCLUSION

We have analytically and numerically investigated a vortex sheet motion in the Richtmyer-Meshkov instability with cylindrical geometry. There exist little differences between analytical calculations and numerical computations with the regularized parameter $\delta=0$ (see Figs. 1 and 2). The agreement between the analytical results and numerical ones for small normalized time shows the accuracy of this numerical method.

We have calculated mode expansions up to the third order in cylindrical geometry and discussed their differences from those in planar geometry. We have also presented that the existence of nonoscillation terms in the perturbation is essential for incompressible fluids in cylindrical geometry. The difference becomes large for low mode. For low mode, nonlinear evolution is mainly determined from either outgoing or ingoing growth rather than spike or bubble. For Atwood number and mode number that satisfy the condition $(An+1)>0$, the ingoing growth is always larger than the outgoing growth in the weakly nonlinear regime. However, in the fully nonlinear regime, i.e., for the normalized time $v_0 t/r_0 > 1$, the ingoing growth rate rapidly decreases and tends to zero, while the outgoing growth rate remains a relatively large value. Concerning to dependence of the growth rates on Atwood number in both weakly and fully nonlinear regimes, the growth rate of spikes increases with the increase of Atwood number, especially that of the ingoing spikes. However, the growth rate of bubbles has relatively weak dependence on Atwood number at least in the weakly nonlinear regime. Even in cylindrical geometry the curvature of spike is larger than that of bubble independently the sign of Atwood number. Both the circulation and sheet strength are large for the case of $A>0$, i.e., a light fluid is surrounded by a heavy fluid, compared with the opposite case.

APPENDIX A

In this Appendix we derive a general form of the nonoscillation part in the perturbation $\eta(\theta,t)$. Since we consider the incompressible fluids, the area S surrounded by the interface must be preserved. This indicates that the area surrounded by the corrugated interface equals to the initial area π:

$$S = \pi = \frac{1}{2}\int_0^{2\pi}\left[1 + \sum_{n=1}^{\infty}\epsilon^n[\eta^{(n)}(\theta,t)]\right]^2 d\theta. \quad (A1)$$

The nonzero parts in the integral with respect to $\eta^{(n)}$ in Eq. (A1) are all produced by the zeroth mode $\eta_0^{(2m)}$ in the even order terms $\eta^{(2m)}$ $(n=2m)$. Taking this into account, Eq. (A1) is rewritten as

$$\frac{1}{2\pi}\int_0^{2\pi}\left[\epsilon^2((\eta^{(1)})^2 + 2\eta^{(2)}) + \epsilon^4[(\eta^{(2)})^2 + 2\eta^{(1)}\eta^{(3)} + 2\eta^{(4)}]\right.$$

$$\left. + \cdots + \epsilon^{2m}\left(\sum_{k=1}^{2m-1}\eta^{(k)}\eta^{(2m-k)} + 2\eta^{(2m)}\right) + \cdots\right]d\theta = 0. \quad (A2)$$

Solving this equation order by order, we get the nonoscillation part $\eta_0^{(2)}$ at $O(\epsilon^2)$

$$\eta_0^{(2)} = -\frac{1}{4}(\eta^{(1)})^2 = -\frac{t^2}{4}, \qquad (A3)$$

where we used the fact that the nonzero part in the integral with respect to $(\eta^{(1)})^2$ is only derived from the term $1/2$ in $\cos^2 n\theta = (1+\cos n\theta)/2$, and we set $\eta(\theta,0) = a_0 \cos n\theta$ and $\partial\eta(\theta,0)/\partial t = \cos n\theta$. We see that Eq. (A3) coincides with $\eta_0^{(2)}$ in Eq. (2.7) derived from the perturbation expansions of the governing equations (2.1)–(2.3).

The fourth order $O(\epsilon^4)$ yields

$$\eta_0^{(4)} = -\frac{1}{4}[2(\eta_0^{(2)})^2 + (\eta_2^{(2)})^2 + 2\eta^{(1)}\eta_1^{(3)}]$$

$$= \frac{t^4}{48}\left[(A^2+1)n^2 - 7An - \frac{45}{4}\right]$$

$$+ \frac{a_0 t^3}{12}\left[(A^2+1)n^2 - \frac{An}{4} - \frac{27}{4}\right]$$

$$+ \frac{a_0^2 t^2}{4}\left[n^2 + \frac{(A+1)n}{4} - 3\right],$$

under the same initial condition as in Eq. (A3).

Generally, we obtain at $O(\epsilon^{2m})$

$$\eta_0^{(2m)} = -\frac{1}{4}\big[\eta^{(1)}\eta_1^{(2m-1)} + (\eta_2^{(2)}\eta_2^{(2m-2)} + 2\eta_0^{(2)}\eta_0^{(2m-2)}) + \cdots$$

$$+ \begin{cases} \displaystyle\sum_{l=0}^{\frac{k-1}{2}} \eta_{k-2l}^{(k)}\eta_{k-2l}^{(2m-k)} & (k:\text{ odd}) \\ \displaystyle\sum_{l=0}^{\frac{k}{2}} \eta_{k-2l}^{(k)}\eta_{k-2l}^{(2m-k)} + \eta_0^{(k)}\eta_0^{(2m-k)} & (k:\text{ even}) \end{cases} + \cdots + (\eta_2^{(2m-2)}\eta_2^{(2)} + 2\eta_0^{(2m-2)}\eta_0^{(2)}) + \eta^{(2m-1)}\eta_1^{(1)}\big]$$

$$= -\frac{1}{4}\sum_{k=1}^{\left[\frac{m+3}{2}\right]} \begin{cases} \displaystyle\sum_{l=0}^{\frac{k-1}{2}} \eta_{k-2l}^{(k)}\eta_{k-2l}^{(2m-k)} & (k:\text{ odd}), \\ \displaystyle\sum_{l=0}^{\frac{k}{2}} \eta_{k-2l}^{(k)}\eta_{k-2l}^{(2m-k)} + \eta_0^{(k)}\eta_0^{(2m-k)} & (k:\text{ even}), \end{cases} \qquad (A4)$$

where $[\cdots]$ is Gauss's symbol and the subscript in η denotes the mode in the superscript order. The initial condition is always taken that $\eta(\theta,0) = a_0 \cos n\theta$ and $\partial\eta(\theta,0)/\partial t = \cos n\theta$ for the higher modes.

APPENDIX B

In this Appendix we derive the governing equation (3.1) for numerical computations. The Bernoulli equation (2.1) can be rewritten as the following equation for the circulation $\Gamma = \phi_1 - \phi_2$ on the interface [11,12]:

$$\frac{d\Gamma}{dt} = 2A\frac{d\Phi}{dt} - A\mathbf{q}\cdot\mathbf{q} + \frac{A-2\alpha}{4}\boldsymbol{\kappa}\cdot\boldsymbol{\kappa} + \alpha A\boldsymbol{\kappa}\cdot\mathbf{q}, \quad (B1)$$

where $\mathbf{q} = (\mathbf{u_1} + \mathbf{u_2})/2$ is an average of the velocities of two fluids at the interface, which is related to the average velocity potential $\Phi = (\phi_1 + \phi_2)/2$ with $\mathbf{q} = \nabla\Phi$.

The circulation Γ is related to the vorticity per unit length Ω at coordinate X on the vortex sheet as

$$\boldsymbol{\Omega} = -\mathbf{n}\times\boldsymbol{\nabla}_{\text{int}}\Gamma = -\mathbf{n}\times\boldsymbol{\kappa} = \kappa\hat{\mathbf{e}}_z, \qquad (B2)$$

where $\boldsymbol{\kappa} = \boldsymbol{\nabla}_{\text{int}}\Gamma$, $\mathbf{n}$ is the unit normal vector at the interface, $\boldsymbol{\nabla}_{\text{int}}$ denotes the gradient at the interface, $\hat{\mathbf{e}}_z$ is the unit vector of the z direction and $\kappa = |\boldsymbol{\kappa}|$. Note that $\boldsymbol{\nabla}_{\text{int}}\Gamma$ is a two-dimensional vector here. The artificial parameter α with $\alpha \neq 0$ for $A \neq 0$ [12,18,19] is related to the tangential velocity of two fluids at the interface. The Lagrange differentiation d/dt in Eq. (B1) is defined as $d/dt = \partial/\partial t + \bar{\mathbf{u}}\cdot\boldsymbol{\nabla}$, where $\bar{\mathbf{u}}$ is given as $\bar{\mathbf{u}} = \mathbf{q} + \alpha\boldsymbol{\kappa}/2$.

Now we introduce the vector potential $\mathbf{B}$ for the velocity field $\mathbf{q}$ as $\mathbf{q} = \nabla\times\mathbf{B}$. Then we have $\nabla\times\mathbf{q} = -\triangle\mathbf{B} = \boldsymbol{\omega}$, where $\boldsymbol{\omega} = \nabla\times\mathbf{q}$ is the vorticity in the system, $\triangle$ is the two-dimensional Laplacian and we took the gauge that $\boldsymbol{\nabla}\cdot\mathbf{B} = 0$. Since we assume that the vorticity distributes only on the interface, i.e., on a vortex sheet, the vorticity $\boldsymbol{\omega}$ is given as

$$\boldsymbol{\omega}(\mathbf{x}) = \int_C \boldsymbol{\Omega}(X(s))\,\delta(\mathbf{x}-X(s))ds, \qquad (B3)$$

for a vortex sheet C with the length parameter s, where δ is the Dirac's delta function. With this $\boldsymbol{\omega}$, the vector potential $\mathbf{B}$ can be written as

$$\boldsymbol{B} = -\frac{1}{2\pi} \int \boldsymbol{\omega}(\boldsymbol{x}')\ln|\boldsymbol{x} - \boldsymbol{x}'|d^2\boldsymbol{x}'. \tag{B4}$$

Taking Eqs. (B2) and (B3) into account and taking the curl of Eq. (B4) with cylindrical coordinates $\boldsymbol{x} = (r, \theta)$, we obtain the two-dimensional Bior-Savart law for the vortex induced velocity $\boldsymbol{q} = (q^r, q^\theta)$:

$$q^r = \frac{-1}{2\pi}\int_0^{2\pi} \frac{\kappa'[r'\sin(\theta - \theta')]s_\beta'd\beta'}{r^2 - 2rr'\cos(\theta - \theta') + r'^2},$$

$$q^\theta = \frac{1}{2\pi}\int_0^{2\pi} \frac{\kappa'[r - r'\cos(\theta - \theta')]s_\beta'd\beta'}{r^2 - 2rr'\cos(\theta - \theta') + r'^2} \tag{B5}$$

(for β, refer to Sec. III).

Now we define the velocity of the cylindrical vortex sheet $\bar{\boldsymbol{u}} = (\bar{u}^r, \bar{u}^\theta)$ as

$$r_t \equiv \bar{u}^r = q^r + \frac{\alpha\kappa r_\beta}{2s_\beta},$$

$$r\theta_t \equiv \bar{u}^\theta = q^\theta + \frac{\alpha\kappa r\theta_\beta}{2s_\beta}, \tag{B6}$$

following the planar case [12,18]. Equation (B6) corresponds to the Birkhoff-Rott equation [20] in planar geometry which describes the velocity of the vortex sheet. Differentiating Eq. (B1) with respect to β and taking the relation $\kappa = \partial\Gamma/\partial s = \Gamma_\beta/s_\beta$ [20] into account, we obtain the following Fredholm integral equation of the second kind:

$$\kappa_t = -\frac{2A}{s_\beta}(r_\beta q_t^r + r\theta_\beta q_t^\theta) - \frac{(1 - \alpha A)}{s_\beta^2}\kappa[(r_\beta q_\beta^r + r\theta_\beta q_\beta^\theta)$$

$$+ (rq^r\theta_\beta^2 - r_\beta\theta_\beta q^\theta)] - \frac{A - \alpha}{4s_\beta}(\kappa^2)_\beta. \tag{B7}$$

This equation exactly coincides with the Euler equation when we choose the factor α as $\alpha = -A$ for $A > 0$ and $\alpha = A$ for $A < 0$, respectively [4,11]. By solving Eqs. (B6) and (B7) numerically, we can determine motion of the cylindrical vortex sheet in RMI.

When we calculate up to the roll-up of the vortex sheet, we regularize the term $r^2 - 2rr'\cos(\theta - \theta') + r'^2$ which appears in denominators in Eq. (B5) as $r^2 - 2rr'\cos(\theta - \theta') + r'^2 + \delta^2$ with a regularized parameter $\delta \ll 1$ introduced by Krasny [16]. This regularization with $\delta \neq 0$, called the vortex method, enables us to compute the evolution of a vortex sheet for a long time. In numerical computations, we expand all dependent variables r, θ, and κ including their β derivatives into the Fourier series [12] and use the filtering technique introduced by Krasny [21]. This is a technique that Fourier amplitudes of the dependent variables under some value set to zero every time step in the temporal integration. This filter cuts the irregular motion due to the round-off error

and enables us to perform the long-time computations. The filter level is set to 10^{-13} (double-precision calculations) throughout this paper. For the temporal integration, we use the fourth-order Runge-Kutta scheme.

The Fredholm equation of the second kind Eq. (B7) is solved by iteration until convergence within some tolerance (10^{-8} here). The trapezoidal rule is adopted for the spatial integration with respect to β when the regularized parameter $\delta \neq 0$. For $\delta = 0$, we use the alternate point quadrature method presented by Sidi and Israeli [22]. This is a quadrature method for calculating singular integrals such as Eq. (B5) with exponential accuracy, in which we can set $\delta = 0$. When we use this method, we choose the parameter $\alpha = -A$ for $A > 0$ and $\alpha = A$ for $A < 0$, respectively. In calculations for $\delta \neq 0$, we choose another α (see Sec. III).

If we perform numerical calculations using the trapezoidal rule with $\delta = 0.1$, the growth rates at $t = 0$ for modes $n = 2$ and $n = 3$ deviate approximately 18 and 26 % from the analytical value of ± 1, and the deviation becomes large for larger mode numbers.

As the Atwood number becomes larger, the numerical calculation becomes harder for both $\delta = 0$ and $\delta \neq 0$. In planar geometry with large Atwood numbers, it is effective for the long-time computations to make the factor α smaller or to use the grid redistribution method such that grid points are arranged equidistantly [12]. However, these methods, especially the latter method, have little effect in cylindrical geometry. In the computations in cylindrical geometry, the clustering at spikes as found in planar geometry with larger Atwood numbers [12,15] is not observed due to, probably, its geometrical property. Therefore, a technique such as the grid redistribution method, which corresponds to give a kind of diffusion to the system, may not be useful.

On the contrary to the case for $\delta = 0$ (see Fig. 1), time until the break-down of the computation for $\delta \neq 0$ with higher mode is longer than that with lower mode when we compare it with the same Atwood number, i.e., a vortex sheet with higher mode number is more stable than that with lower mode. In addition to that, there is a tendency that a vortex sheet which the inner fluid is heavier than the outer fluid ($A < 0$) is more stable and long-lived than the reverse one ($A > 0$) for a fixed mode number $n \leq 3$ and the same Atwood number in its absolute value. When the mode $n \geq 4$, there is no difference in the break-down time between $A > 0$ and $A < 0$ for the same Atwood number in its absolute value for $0 \leq |A| \leq 0.2$. The break-down times with $\delta = 0.1$ were $t = 0.7$, 1, 4, and 2.2 for $n = 1$, 2, and 3, respectively, and $t = 3.2$ for $4 \leq n \leq 8$ when $A = 0.2$, while $t = 0.8$ for $n = 1$ and $t = 3.2$ for $2 \leq n \leq 8$ when $A = -0.2$. These break-down times in the corresponding modes were almost unchanged over the range $0 \leq |A| \leq 0.2$ for both cases of $A > 0$ and $A < 0$. When the Atwood number becomes larger in its absolute value, the break-down time becomes shorter for the corresponding mode for both cases of $A > 0$ and $A < 0$.

[1] R. D. Richtmyer, Commun. Pure Appl. Math. **13**, 297 (1960); E. E. Meshkov, Fluid Dyn. **4**, 101 (1969).

[2] Q. Zhang and M. J. Graham, Phys. Rev. Lett. **79**, 2674 (1997).

[3] V. Zhakhovskii, K. Nishihara, and M. Abe, *Inertial Fusion Sciences and Applications 2001* (Elsevier, Amsterdam, 2002), pp. 106.

[4] C. Matsuoka and K. Nishihara, Phys. Rev. E **73**, 055304(R) (2006).

[5] R. Kishony and D. Shvarts, Phys. Plasmas **8**, 4925 (2001).

[6] M. A. Jones and J. W. Jacobs, Phys. Fluids **9**, 3078 (1997).

[7] N. E. Lanier *et al.*, Phys. Plasmas **10**, 1816 (2003).

[8] J. R. Fincke *et al.*, Phys. Rev. Lett. **93**, 115003 (2004), and references therein.

[9] S. H. R. Hosseini, T. Ogawa, and K. Takayama, J. Visualization **2**, 371 (2000); S. H. R. Hosseini and K. Takayama, Phys. Fluids **17**, 084101 (2005).

[10] A. L. Velikovich *et al.*, Phys. Plasmas **7**, 1662 (2000), and references therein.

[11] C. Matsuoka, K. Nishihara, and Y. Fukuda, Phys. Rev. E **67**, 036301 (2003).

[12] C. Matsuoka and K. Nishihara, Phys. Rev. E **73**, 026304 (2006), and references therein.

[13] Q. Zhang and S. Sohn, Phys. Fluids **9**, 1106 (1997).

[14] A. D. Kotelnikov, J. Ray, and N. J. Zabusky, Phys. Fluids **12**, 3245 (2000).

[15] S. I. Sohn, Phys. Rev. E **69**, 036703 (2004).

[16] R. Krasny, J. Fluid Mech. **184**, 123 (1987).

[17] S. I. Abarzhi, K. Nishihara, and J. Glimm, Phys. Lett. A **317**, 470 (2003).

[18] G. R. Baker, D. I. Meiron, and S. A. Orszag, J. Fluid Mech. **123**, 477 (1982).

[19] D. I. Pullin, J. Fluid Mech. **119**, 507 (1982).

[20] P. G. Saffman, in *Vortex Dynamics* (Cambridge University Press, Cambridge, 1992), pp. 141.

[21] R. Krasny, J. Comput. Phys. **65**, 292 (1986).

[22] A. Sidi and M. Israeli, J. Sci. Comput. **3**, 201 (1988).